

The Photoisomerization Mechanism of Azobenzene: A Semiclassical Simulation of Nonadiabatic Dynamics

Cosimo Ciminelli, Giovanni Granucci, and Maurizio Persico*^[a]

Abstract: We have simulated the photoisomerization dynamics of azobenzene, taking into account internal conversion and geometrical relaxation processes, by means of a semiclassical surface hopping approach. Both $n \rightarrow \pi^*$ and $\pi \rightarrow \pi^*$ excitations and both *cis* \rightarrow *trans* and *trans* \rightarrow *cis* conversions have been considered. We show that in all cases the torsion around the N=N double bond is the preferred mechanism. The quantum yields measured are correctly reproduced and the observed differences are explained as a result of the competition between the inertia of the torsional motion and the premature deactivation of the excited state. Recent time-resolved spectroscopic experiments are interpreted in the light of the simulated dynamics.

Keywords: azobenzene • nonadiabatic dynamics • photoisomerization • semiclassical wavepacket dynamics • semiempirical calculations

Introduction

Azobenzene and its derivatives are one of the most important classes of photochromic compounds. Their reversible photoisomerization is the basis for a great variety of nanoscale devices and materials with photomodulable properties.^[1–14] A great variety of properties and functions can be made photoswitchable: structure and self-organization of materials, chemical and biochemical activity, optical, electrical and permeation parameters. For many of these applications one of the basic concerns is that the photoisomerization quantum yields may be lowered by the inclusion of azobenzene in rather constraining molecular environments. Also important, in some cases, is the overall response time, that is, the time required for the photoisomerization and the (following or simultaneous) reorganization of the whole supramolecular system (see e.g. refs. [1, 15]).

Such features of the processes taking place in the excited and ground states depend on the detailed reaction mechanism and can be studied by semiclassical simulation methods,^[16] as shown in this paper. Understanding the photoisomerization mechanism of azobenzene is an interesting basic issue in itself, and is also instrumental to the design of better nanoscale devices. Simulations of supramolecular systems can also be carried out, with a QM/MM extension of

the method here applied:^[17–19] however, the most advanced time-resolved spectroscopic techniques have been applied to azobenzene itself, so this will be the first benchmark for the simulation results.

The spectroscopy and photochemistry of *cis*- and *trans*-azobenzene (in the following referred to as CAB and TAB) have been summarized in several reviews.^[20–23] An important feature to be explained is that the photoisomerization quantum yields for $n \rightarrow \pi^*$ excitation, at 380–500 nm, considerably exceed those obtained by $\pi \rightarrow \pi^*$ excitation, at 280–380 nm, for both the *cis* \rightarrow *trans* and *trans* \rightarrow *cis* reactions. This led to the hypothesis that different mechanisms operate in the two cases. Potential energy curves for the two envisageable pathways, torsion of the N=N double bond and N-inversion (see Figure 1), were computed by Monti et al.^[24] as early as in 1982, for three singlet states at CI (configuration interaction) level with a minimal basis set. These results indicated that inversion should be the preferred pathway in S_1 , corresponding to the $n \rightarrow \pi^*$ excitation, and torsion in S_2 . Experimental support for this hypothesis was found by Rau and co-workers, who studied the photoisomerization of cyclic and sterically hindered azobenzenes.^[21, 25, 26] However, more accurate computational studies^[27, 28] have recently shown that the shape of the potential energy surfaces (PES) is rather different from what previously believed. Namely, the shape of the S_1 PES is more favourable to torsion than to inversion; moreover, a fourth singlet PES (S_3 state), with a pronounced minimum around $\angle \text{CNNC} = 90^\circ$, crosses that of S_2 along the torsion pathway and is therefore important for the dynamics following $\pi \rightarrow \pi^*$ excitation. Unpublished results by Diau^[29] and by Orlandi group^[30, 31] substantially

[a] Dr. C. Ciminelli, Dr. G. Granucci, Prof. M. Persico
Dipartimento di Chimica e Chimica Industriale
Università di Pisa, v. Risorgimento 35
56126 Pisa (Italy)
E-mail: mau@dcc.unipi.it

confirm these findings, while shedding light on previously unnoticed features of the PES and of the crossing seams.

The new theoretical results therefore challenge the original, widely accepted, mechanistic interpretation of the photoisomerization of azobenzene. Starting with 1996, there has been a flourishing of time-resolved spectroscopic experiments on this reaction,^[32–40] which detected transients with lifetimes ranging from about 0.1 to 10–20 ps. The discussion of most of these results, with the exception of the most

pretation of several time-resolved spectroscopic studies, in the light of our computational results.

Method and Semiempirical Representation of the Electronic States

In this work we have applied a direct semiclassical dynamics approach recently developed in our group^[16] and imple-

mented in a development version of the MOPAC package.^[42]

The method combines Tully's trajectory surface hopping approach^[43] with a direct semiempirical calculation of PES and electronic wavefunctions. The direct or "on the fly" strategy avoids the cumbersome fitting or interpolation procedures for the preparation of analytic PES and other electronic matrix elements, and is practically mandatory for systems such as azobenzene, where at least five internal coordinates undergo large amplitude variations (CNNC and CCNN dihedrals and NNC angles).

The choice of a semiempirical method for solving the electronic problem is apparently the best compromise between accuracy, transferability and computing speed. An acceptable level of accuracy, also for the excited state PES, was reached by re-optimizing the semiempirical parameters, as described below. In practice, for molecules of the size of azobenzene, the re-parametrized semiempirical PES are as accurate as the best available ab initio ones.^[27–31,41] The parameters are fairly transferable,^[18] in the

sense that standard or reoptimized sets can be trusted to yield quite acceptable results for all the details of the PES which are not of primary importance for the process under study (for instance, CH stretching and CCH bending potentials in azobenzene).

In order to represent excited states and to treat highly distorted geometries, the electronic wavefunctions were of the CI type. The molecular orbitals (MO) were obtained by means of a modified SCF procedure with floating occupation numbers (ON).^[16,44] Thus, the MO occupation was continuously adapted to the geometry: for instance, when the π and π^* orbitals become almost degenerate because of the double bond torsion, their ON were almost equal. Moreover, the lowest virtual MOs were partially optimized, as in

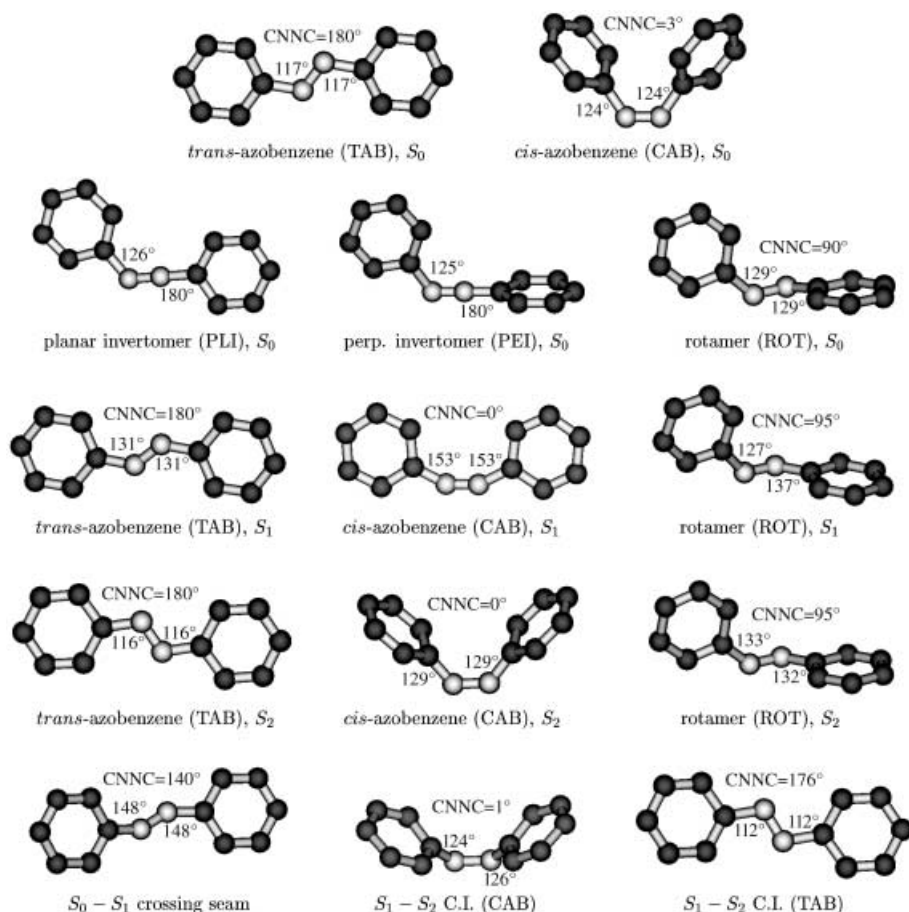


Figure 1. Optimized geometries for ground and excited states (indicated S_N) and conical intersections (indicated S_N-S_{N+1} C.I.). The following constraints were imposed: $\nless CNNC=180^\circ$ for TAB S_1 and S_2 ; $\nless CNNC=0^\circ$ for CAB S_1 and S_2 ; $\nless CNNC=140^\circ$ for the S_0-S_1 crossing seam; $\nless NNC=180^\circ$ for PLI and PEI.

recent ones,^[39] was inevitably unaware of the almost contemporary theoretical progresses, but some new ideas were put forward. However, a thorough explanation of the experimental evidence is still missing, and we think it can only derive from a study of the reaction dynamics, including non-adiabatic transitions between the first four singlet states. This is the aim of the present work. In the next section we specify the essential details of the semiempirical method and we outline the most important features of the potential energy surfaces (PES). We will then describe the results of the simulations, with emphasis on the reaction mechanism (torsion versus inversion) and on the dynamical effects which influence the quantum yields. Finally, in the last section before the concluding remarks, we shall offer an inter-

a state-averaged CASSCF calculation. The CI space was a complete active space with four electrons in four MOs, corresponding to the highest n and π and the two lowest π^* at undistorted geometries. In addition, the CI includes all single excitations involving the last five occupied MOs and the first five virtuals. The total number of determinants was 259.

Target values of energies and geometrical parameters used in the optimization of the semiempirical parameters are listed in Table 1, along with the final results obtained with the semiempirical wavefunctions. Details of the procedure are given in Appendix A. Table 2 reports the vertical transition energies computed with a variety of methods. It is apparent that the re-parametrized semiempirical calculation competes in accuracy with the best ab initio methods.

Figures 2 and 3 show the potential energy curves of four singlets and two triplets along the torsion and inversion reaction pathways. In Figure 2, the angle $\phi = \angle \text{CNNC}$ is

Table 1. Target values for the optimization of the semiempirical parameters and corresponding values computed at semiempirical level. Energies in eV, referred to TAB S_0 if not otherwise specified; distances in Å, angles in degrees.

	Semiempirical	Target
vertical excitation energies		
TAB S_1	2.94	2.81
TAB S_2	4.28	3.90
TAB S_3	4.80	3.90
TAB T_1	1.78	2.09
TAB T_2	2.89	2.83
CAB S_1	3.23	2.81
CAB S_2	5.03	4.60
CAB S_3	5.00	4.60
CAB T_1	3.73	4.69
CAB T_2	3.66	4.75
energies at other geometries		
$E(\text{CAB}) - E(\text{TAB}); S_0$	0.40	0.66
$E(\text{ROT}) - E(\text{PEI}); S_0$	0.28	0.29
PEI, S_0 (opt. S_0)	1.76	2.08
PEI, S_1 (opt. S_0)	3.37	3.31
PEI, S_2 (opt. S_0)	6.48	5.09
PEI, S_3 (opt. S_0)	6.92	7.35
PEI, T_1 (opt. S_0)	2.34	3.02
PEI, T_2 (opt. S_0)	5.49	6.30
PLI, S_0 (opt. S_0)	1.95	2.91
ROT, S_0 (opt. S_0)	2.05	2.37
ROT, S_1 (opt. S_1)	2.48	2.88
equilibrium geometries		
TAB, R_{NN}	1.239	1.247
TAB, R_{NC}	1.427	1.428
TAB, $\angle \text{NNC}$	117.5	114.1
CAB, R_{NN}	1.221	1.253
CAB, R_{NC}	1.434	1.449
CAB, $\angle \text{NNC}$	124.3	121.9
CAB, $\angle \text{CNNC}$	4.1	6.5
CAB, $\angle \text{NNCC}$	54.7	53.3

Table 2. Vertical transition energies [eV] obtained by several methods.

method	TAB			CAB		
	S_1	S_2	S_3	S_1	S_2	S_3
semiemp. (this work)	2.94	4.28	4.80	3.23	5.03	5.00
CIPSI ^[a]	2.81	4.55	4.61	2.94	4.82	4.86
CASSCF 6e ⁻ /5 MO	3.48	6.26	6.37	4.53	6.80	6.37
MRSDCI ^[b]	3.11	5.39	6.56	3.95	6.12	5.56
CASSCF 10e ⁻ /10 MO ^[c]	3.11	5.56	5.66			
CASPT2 ^[c]	2.34	4.74	4.81			
CASSCF 14e ⁻ /12 MO ^[d]	3.18			3.38		
CASPT2 ^[e]	2.70	3.95	4.12			
exp. ^[33,34,37]	2.80	3.94		2.86	4.38	

[a] Multireference perturbation theory with selected zero-order space; reduced 6-31G basis set with polarization functions on N.^[27] [b] Multireference singles and doubles CI; split-valence basis set with polarization functions on N.^[28] [c] 6-31G basis set.^[41] [d] 6-31G* basis set.^[31] [e] ANO basis set, 3s2p1d for C and N, 2s1p for H. Based on 14e⁻/12 MO CASSCF.^[30]

varied, and all other internal coordinates are optimized; the optimization was carried out independently for S_0 , S_1 and S_2 . For the inversion pathway we take $\theta_1 = \angle \text{CN}_1\text{N}_2$ as the independent variable, and we minimize the energies of S_0 and S_1 . In the ground state, the phenyl group which migrates remains in the CNNC plane only at transoid geometries ($\theta_1 < 130^\circ$), then it rotates to approach the perpendicular invertomer geometry (see Figure 1). Note that the torsion curves can be labelled with C_2 symmetry symbols, which makes apparent the presence of a crossing seam between S_2 and S_3 , whereas no symmetry element is conserved upon inversion. Overall, the S_1 and S_2 surfaces are quite similar to those computed by Ishikawa et al.,^[28] who made the most extensive exploration of the azobenzene PES, at CASSCF level. However, our semiempirical S_2 and S_3 energies are lower than theirs, and closer to previous ab initio results obtained with more extensive CI treatments.^[27,30,31,41]

Figure 1 and Table 3 show the essential features of some of the most important structures: global, local and constrained minima, transition states, and conical intersections. In some of the optimizations the CNNC or NNC angles have been constrained to fixed values, in order to locate approximately transition states or transoid/cisoid minima. Namely, we obtain conditioned minima of the latter kind for S_1 and we find a considerable symmetric opening of the NNC angles: the difference with respect to the equilibrium values in S_0 is about 14° for TAB and 29° for CAB. This is clearly due to the decrease of electronic charge in the nonbonding orbitals. In S_2 the optimal NNC angles undergo much smaller changes with respect to the ground state.

The conical intersections are of the highest interest for the nonadiabatic dynamics. Crossing seam optimizations have been performed by means of a new algorithm based on a penalty function (see Appendix B). We optimized successfully five conical intersections (see Figure 2). One involves S_0 and S_1 and coincides with the minimum in the excited state, at $\angle \text{CNNC} \approx 95^\circ$: it is therefore a very efficient funnel. Two conical intersections between S_1 and S_2 have been located at transoid and cisoid geometries, respectively, and are very close to the minimum energy path in S_2 ; small geometrical distortions and almost negligible increases in the S_2 energy are needed to access them. Also along the S_2/S_3 crossing seam we find two minima: one at a transoid ge-

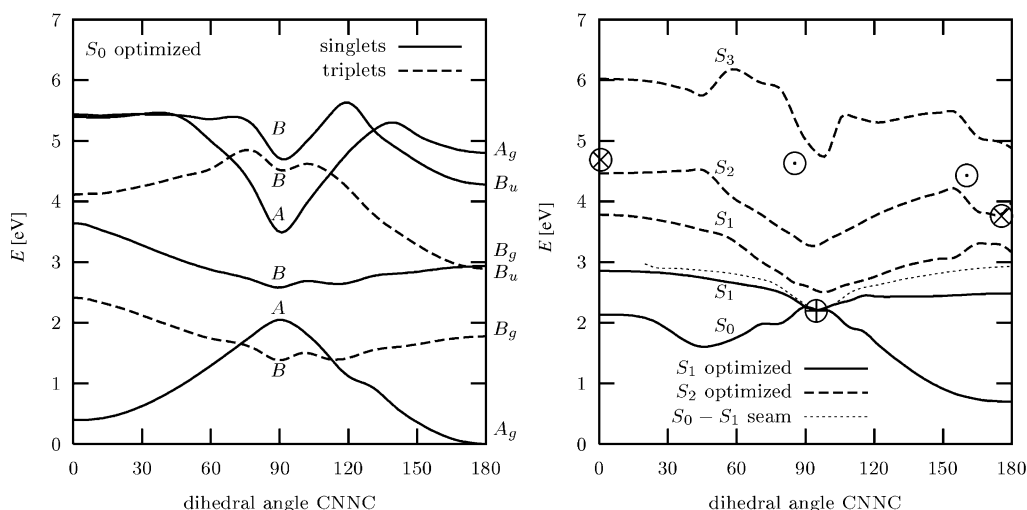


Figure 2. Potential energy curves for the torsion around the N=N bond. All internal coordinates are optimized as the angle CNNC is varied. Left panel: the S_0 energy is minimized and the other energies are computed at the S_0 optimal geometry; right panel: same for S_1 and S_2 . Circles indicate position and energy of optimized conical intersections: \oplus , S_0 - S_1 ; \otimes , S_1 - S_2 ; \odot , S_2 - S_3 . The dotted line corresponds to the S_0 - S_1 crossing seam.

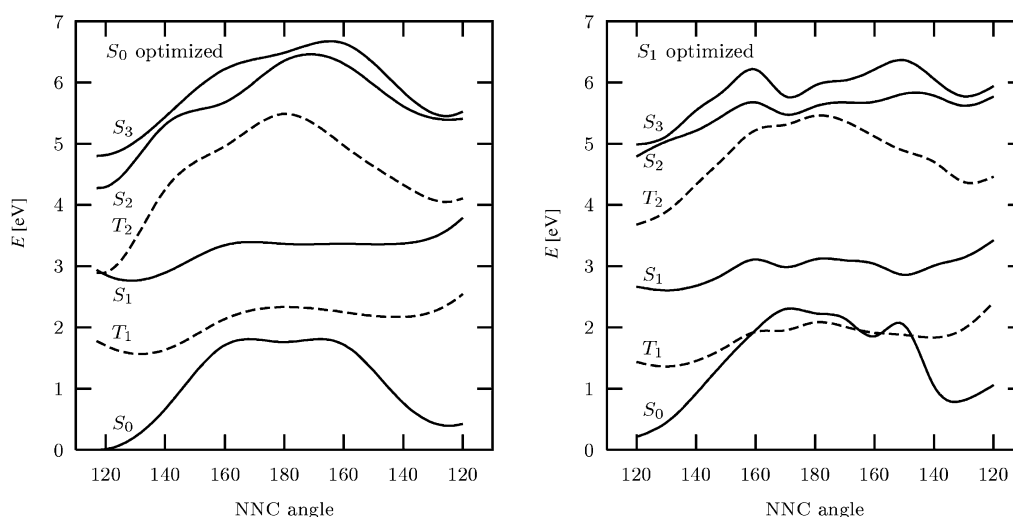


Figure 3. Potential energy curves for the N inversion. All internal coordinates are optimized as one of the NNC angles is varied. Left panel: the S_0 energy is minimized and the other energies are computed at the S_0 optimal geometry; right panel: same for S_1 .

Table 3. Energies and geometries of important points in the azobenzene PES, computed at semiempirical level. Energies with respect to ground state TAB (global minimum), in eV. Distances in Å, angles in degrees.

Structure	State ^[a]	<i>E</i>	<i>R</i> _{NN}	∠NNC ^[b]	∠CNNC
TAB	S_0	0.00	1.239	117.5	180.0
CAB	S_0	0.40	1.221	124.3	4.1
ROT	S_0	2.05	1.244	129.5	90.0 ^[c]
PEI	S_0	1.76	1.205	125.0/180.0 ^[c]	–
TAB	S_1	2.48	1.202	131.5	180.0 ^[c]
CAB	S_1	2.85	1.230	152.9	0.0 ^[c]
ROT	S_1	2.20	1.231	126.8/137.0	95.0
TAB	S_2	3.99	1.283	116.5	180.0 ^[c]
CAB	S_2	4.46	1.283	129.3	0.0 ^[c]
ROT	S_0/S_1	2.20	1.232	126.3/136.5	94.7
TAB	S_0/S_1	2.93	1.208	152.4	180.0 ^[c]
TAB	S_1/S_2	3.76	1.289	112.0	175.8
CAB	S_1/S_2	4.69	1.329	125.1	0.7
TAB	S_2/S_3	4.43	1.284	119.9/122.6	160.6
ROT	S_2/S_3	4.63	1.254	129.3/136.0	85.5

[a] One state label indicates a PES minimum; two states indicate a conical intersection. [b] We report two different values for asymmetric geometries. [c] Constrained internal coordinate.

ometry ($\angle \text{CNNC} \cong 160^\circ$) and the other one at about half way of the torsional reaction path ($\angle \text{CNNC} \cong 85^\circ$).

After this work was completed we became aware of unpublished results by Diau^[29] and by Orlandi group.^[30,31] Both confirm the existence of the S_0 - S_1 conical intersection and its asymmetric geometry. Gagliardi et al.^[30] performed rather accurate CASPT2 calculations, based on a 14 e^- /12 MO CASSCF with a double zeta basis plus polarization functions on C, N and H. They found the

twisted minimum of the 2^1A state (S_2 or S_3 at other geometries) slightly lower than 1^1B (S_1), as far as the presence of a C_2 axis allows one to attribute different symmetry labels to the two states. Since the minimum is located at $\angle \text{CNNC} \cong 100^\circ$, the authors propose that torsion within the S_2 – S_3 manifold is the mechanism of *trans*→*cis* photoisomerization, with low quantum yield because of a fast decay to S_0 at unfavourable geometries. Diau^[29] explored three reaction pathways by CASSCF calculations: torsion, inversion and double inversion, that is, symmetric opening of the NNC angles (starting from TAB). He found, along the last coordinate, an S_0 – S_1 conical intersection, with $\angle \text{NNC} \cong 157^\circ$ and energy about 1 eV above the S_1 minimum. Since this funnel becomes accessible with a large vibrational energy excess, Diau proposed that it can play a role in increasing the deactivation rate in the case of π → π^* excitation, thus lowering the quantum yields.

Although the double inversion pathway was not taken into account when optimizing the semiempirical parameters, we found Diau's conical intersection in good agreement with his *ab initio* calculations, at $\angle \text{NNC} \cong 152.4^\circ$ and 0.73 eV above the S_1 minimum. More important, as we shall see at the end of the next section, it turns out that the double inversion conical intersection lies on the same crossing seam as the minimum energy one. Only for CNNC angles close to 90° does the crossing seam coincide approximately with the minimum energy path along the torsional coordinate in S_1 . For other $\angle \text{CNNC}$ values, both on the *cis* and on the *trans* side, a progressive opening of the NNC angles with respect to the S_1 optimum values is needed to cross the S_0 surface. This is due to the shape of the two PES, the S_0 one raising much more than that of S_1 as the NNC angles open. On the other hand, the S_1 PES goes up steeply when closing the NNC angles, and this is why the S_1 – S_2 crossing is found at NNC smaller than optimal for both states.

Simulation of the Photoisomerization Dynamics

We ran four simulations, for the *trans*→*cis* and *cis*→*trans* photoisomerizations, with two different ranges of initial excitation energies: the 2.7–3.7 eV interval (S_1 state of n → π^* character) and the 3.7–5.5 eV one (S_2 – S_3 , π → π^* transition). Each simulation involves more than 200 trajectories, with initial conditions reproducing vertical excitation from a Boltzmann distribution of coordinates and momenta for one of the stable isomers in the ground state (see Appendix C). The distribution of excitation energies, that is, the simulated absorption spectrum, shows two bands. For TAB the bands are centred at 3.16 and 4.41 eV, while for CAB they are at 3.27 and 4.80 eV, with FWHM of about 0.35 eV. These values are all slightly higher than the experimental ones^[33,34,37] (2.80 and 3.94 eV for TAB, 2.86 and 4.38 eV for CAB), but in the right relationships. A comparison with the results of Table 1 shows that in some cases the vertical transition energy is in slightly better agreement with experiment than the maximum of the simulated spectrum: this is simply due to a cancellation of errors.

Each trajectory is stopped when it has reverted to the ground state and has approached the geometry of a stable isomer, either the starting one or the other one. The criterium is that $\angle \text{CNNC}$ should be comprised between -2 and $+2^\circ$ for CAB, or 178 to 182° for TAB. These specifications define a conventional “reaction time” t_R , which goes from the vertical excitation to the end of the trajectory. In the following we shall distinguish between “reactive trajectories”, which start close to the equilibrium geometry of one isomer and end up at the other one; and “unreactive trajectories”, which revert to the initial isomer. Table 4 shows the average t_R for reactive and unreactive trajectories. It is apparent that starting from the less stable isomer, CAB, all the times are shorter. Moreover, exciting to S_2 or S_3 delays the isomerization with respect to the S_1 excitation.

The fraction of reactive trajectories is the computed quantum yield Φ . In Table 5 the computed and experimental quantum yields are compared. The agreement is satisfactory: as expected, $\Phi_{\text{cis} \rightarrow \text{trans}}$ is larger than $\Phi_{\text{trans} \rightarrow \text{cis}}$ and in both cases the n → π^* quantum yield exceeds the π → π^* one. Most of the times the computed quantum yields are close to the upper values of the ranges obtained in different solvents, which is consistent with a moderate inhibiting effect of some solvents on the geometry changes leading to photoisomerization. We have also examined the dependence of the quantum yields on the initial excitation energy. There is no evidence of important variations of the quantum yield within the n → π^* absorption band, while, within the π → π^* band, $\Phi_{\text{trans} \rightarrow \text{cis}}$ shows a slight increase as a function of the excitation energy and $\Phi_{\text{cis} \rightarrow \text{trans}}$ a slight decrease. The relative insensitivity of the quantum yields on the excitation energy (a rather common case in photochemistry) is an indication that small errors in the excited state energetics should not affect too much the calculated results, provided the overall shape of the PES is correct. In the low absorption gap between the two bands we have very few trajectories, so the quantum yields are undetermined. However, our data are consistent with a rather sudden decrease of the quantum yield, in passing from n → π^* to π → π^* excitation, if only for the *trans*→*cis* reaction where this effect is more marked.

The simulations show that the preferred reaction pathway is torsion of the N=N double bond in all four cases (*cis*→*trans* or *trans*→*cis*, n → π^* or π → π^* excitation). This can be seen in Figure 4, where the average CNNC and NNC angles are plotted as functions of time. Of the two NNC angles we chose, for each point along a trajectory, the smaller and the larger one, which contribute to separate averages, so as to bring out the asymmetric opening of one of the two angles, that is, the N inversion, if it would occur. Moreover, we distinguish among reactive and unreactive trajectories. At the beginning, the two CNNC plots are almost coincident, but they start to diverge well before reaching the half-way ($\angle \text{CNNC} = 90^\circ$). Upon excitation in S_1 , the NNC angles tend to open in a symmetric way, as expected since the cisoid and transoid minima of S_1 (see Figure 1 and Table 3) have NNC angles significantly larger than in the ground state. However, the inversion mechanism would require an asymmetric NNC motion, which does not take place: in fact, the NNC angles do oscillate, without going beyond about

Table 4. Simulation results for distinct groups of trajectories: reactive ($trans \rightarrow cis$ or $cis \rightarrow trans$), unreactive ($trans \rightarrow trans$ or $cis \rightarrow cis$) and total (reactive + unreactive), starting from each isomer. t [fs], E [eV], angles [°]. Averages \pm standard deviations are given where appropriate.

Starting from TAB:	$n \rightarrow \pi^*$ excitation (S_1)			$\pi \rightarrow \pi^*$ excitation (S_2/S_3)		
	reactive	unreact.	total	reactive	unreact.	total
number of trajectories	72	143	215	34	188	222
total energy wrt TAB	4.94 ± 0.31	4.95 ± 0.30	4.94	6.18 ± 0.27	6.17 ± 0.33	6.17
vertical transition energy	3.15 ± 0.38	3.17 ± 0.32	3.16	4.46 ± 0.41	4.40 ± 0.43	4.41
initial $\theta = \angle \text{CNNC}$	175 ± 3	176 ± 3	176	175 ± 3	176 ± 3	176
total time t_R	379 ± 193	524 ± 252	475	696 ± 317	543 ± 273	566
time of first hop $S_2 \rightarrow S_1$				47 ± 47	61 ± 52	51
$\theta = \angle \text{CNNC}$ at first hop $S_2 \rightarrow S_1$				174 ± 5	172 ± 5	173
larger $\angle \text{NNC}$ at f. hop $S_2 \rightarrow S_1$				117 ± 4	116 ± 3	116
smaller $\angle \text{NNC}$ at f. hop $S_2 \rightarrow S_1$				113 ± 3	112 ± 3	112
time of last hop $S_1 \rightarrow S_0$	322 ± 152	331 ± 158	328	604 ± 280	407 ± 203	437
$\theta = \angle \text{CNNC}$ at first hop $S_1 \rightarrow S_0$	104 ± 10	113 ± 13	110	111 ± 24	134 ± 22	130
$d\theta/dt$ at first hop $S_1 \rightarrow S_0$	-2.0 ± 1.2	-0.3 ± 1.2	-0.8	-1.7 ± 1.5	-0.3 ± 1.4	-0.6
larger $\angle \text{NNC}$ at f. hop $S_1 \rightarrow S_0$	140 ± 4	139 ± 4	140	141 ± 5	139 ± 9	140
smaller $\angle \text{NNC}$ at f. hop $S_1 \rightarrow S_0$	133 ± 5	132 ± 6	133	133 ± 7	134 ± 9	134
time of last hop $S_1 \rightarrow S_0$	368 ± 186	400 ± 194	389	679 ± 343	452 ± 218	487
$\theta = \angle \text{CNNC}$ at last hop $S_1 \rightarrow S_0$	99 ± 5	121 ± 20	114	95 ± 17	134 ± 24	128
$d\theta/dt$ at last hop $S_1 \rightarrow S_0$	-2.4 ± 1.1	0.2 ± 1.5	-0.6	-1.7 ± 1.6	0.1 ± 1.5	-0.2
Starting from CAB:						
	$n \rightarrow \pi^*$ excitation (S_1)			$\pi \rightarrow \pi^*$ excitation (S_2/S_3)		
	reactive	unreact.	total	reactive	unreact.	total
number of trajectories	140	91	231	153	169	322
total energy wrt TAB	5.47 ± 0.30	5.47 ± 0.28	5.47	7.00 ± 0.27	7.01 ± 0.28	7.00
vertical transition energy	3.28 ± 0.35	3.25 ± 0.33	3.27	4.78 ± 0.38	4.81 ± 0.35	4.80
initial $\theta = \angle \text{CNNC}$	5 ± 3	5 ± 3	5	5 ± 3	5 ± 3	5
total time t_R	214 ± 75	101 ± 42	170	293 ± 112	163 ± 80	225
time of first hop $S_2 \rightarrow S_1$				50 ± 59	59 ± 53	55
$\theta = \angle \text{CNNC}$ at first hop $S_2 \rightarrow S_1$				22 ± 31	24 ± 28	23
larger $\angle \text{NNC}$ at f. hop $S_2 \rightarrow S_1$				125 ± 4	124 ± 3	124
smaller $\angle \text{NNC}$ at f. hop $S_2 \rightarrow S_1$				121 ± 3	121 ± 3	121
time of first hop $S_1 \rightarrow S_0$	62 ± 23	65 ± 27	63	122 ± 72	128 ± 69	125
$\theta = \angle \text{CNNC}$ at first hop $S_1 \rightarrow S_0$	82 ± 4	81 ± 5	82	82 ± 5	79 ± 10	80
$d\theta/dt$ at first hop $S_1 \rightarrow S_0$	1.8 ± 0.9	0.2 ± 1.2	1.2	1.7 ± 1.3	0.1 ± 1.9	0.9
larger $\angle \text{NNC}$ at f. hop $S_1 \rightarrow S_0$	130 ± 3	130 ± 3	130	130 ± 4	131 ± 5	131
smaller $\angle \text{NNC}$ at f. hop $S_1 \rightarrow S_0$	120 ± 4	119 ± 5	120	119 ± 4	120 ± 4	119
time of last hop $S_1 \rightarrow S_0$	88 ± 88	88 ± 51	88	209 ± 148	154 ± 86	180
$\theta = \angle \text{CNNC}$ at last hop $S_1 \rightarrow S_0$	88 ± 16	81 ± 12	85	108 ± 34	80 ± 11	93
$d\theta/dt$ at last hop $S_1 \rightarrow S_0$	1.7 ± 1.0	-0.6 ± 1.5	0.8	0.8 ± 2.2	-0.9 ± 2.1	-0.1

Table 5. Computed and experimental^[21] quantum yields. Statistically derived standard deviations for the theoretical values are given^[a].

	$n \rightarrow \pi^*$ excitation	$\pi \rightarrow \pi^*$ excitation
$\Phi_{trans \rightarrow cis}$, computed	0.33 ± 0.03	0.15 ± 0.02
$\Phi_{trans \rightarrow cis}$, experimental	0.20–0.36	0.09–0.20
$\Phi_{cis \rightarrow trans}$, computed	0.61 ± 0.03	0.48 ± 0.03
$\Phi_{cis \rightarrow trans}$, experimental	0.40–0.75	0.27–0.44

[a] The standard deviation for the quantum yield Φ computed over a total of N_T trajectories is $\sigma = \sqrt{\Phi(1-\Phi)/N_T}$.

140°. Several pronounced oscillations follow the $n \rightarrow \pi^*$ excitation of TAB, while starting from CAB the torsion of the CNNC angle is faster, so there is time only for one oscillation along the NNC coordinate. Notice that the S_1 minimum, where all trajectories are attracted (also those starting in S_2/S_3 , as we shall see), is slightly asymmetric and its NNC angles are intermediate between those of TAB and CAB in S_1 , and larger than in S_0 or S_2 . These remarks explain why, in the case of $\pi \rightarrow \pi^*$ excitation, the NNC averages increase gradually, as they adapt to the S_1 PES after internal conversion (IC).

Since we correctly reproduce the difference in $n \rightarrow \pi^*$ and $\pi \rightarrow \pi^*$ quantum yields, we conclude that the hypothesis of completely different reaction pathways for the two cases can be disposed of. The explanation must be sought in the details of the reaction dynamics. The following analysis will show that the quantum yields are determined by the competition between the $S_1 \rightarrow S_0$ IC and the torsional motion around the N=N double bond: if the IC occurs too early, that is, much before the midpoint along the torsional coordinate ($\angle \text{CNNC} = 90^\circ$), no isomerization occurs, because of the unfavourable slope of the S_0 PES. Excitation in the $\pi \rightarrow \pi^*$ band, with respect to the $n \rightarrow \pi^*$ one, is characterized by a larger available vibrational energy and by the excitation of internal modes which favour the “early IC”, so decreasing the quantum yield.

Figure 5 shows the time dependent populations of the electronic states; for the ground state, we distinguish the *cis* and *trans* pop-

ulations, P_{cis} and P_{trans} , according to the CNNC angle ($-30^\circ < \angle \text{CNNC} < 30^\circ$ for *cis*, $150^\circ < \angle \text{CNNC} < 210^\circ$ for *trans*); note that, with these definitions, in general $P_{cis} + P_{trans} < P_{S_0}$.

In the next section we shall try to correlate the electronic population dynamics with the observation of transients in time-resolved spectroscopic studies.^[32–41] Here we just underline that the S_2 and S_3 states, when populated by $\pi \rightarrow \pi^*$ excitation, undergo a very fast decay to S_1 , within about 100 fs. This is due to the presence of S_1 – S_2 conical intersections very close to the Franck–Condon regions, both on the *trans* and on the *cis* sides (see Figure 2). During such a short time, there is little torsion of the N=N bond, especially when starting from TAB. The torsional motion is indeed slower than with $n \rightarrow \pi^*$ excitation, because of the unfavourable slope of the S_2 and S_3 PES in the Franck–Condon region. This can be seen in Figure 4 and also in Table 4, where we have listed the average $\angle \text{CNNC}$ at the time of the first $S_2 \rightarrow S_1$ surface hopping. The reaction therefore takes place essentially on the S_1 surface, in agreement with evidence obtained by the time-resolved fluorescence studies of Tahara

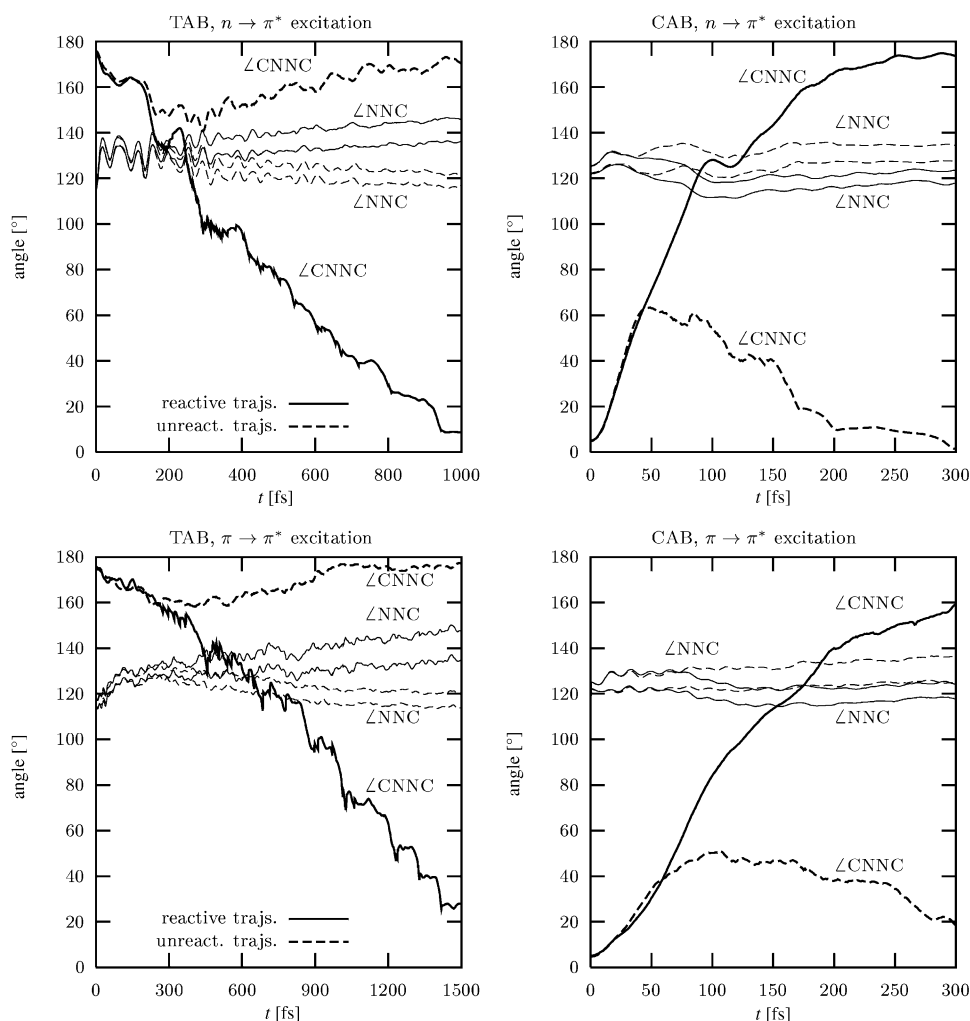


Figure 4. Average CNNC and NNC angles as functions of time, for reactive (*trans*→*cis* or *cis*→*trans*) and unreactive trajectories. Two averages are shown for the NNC angles: one for the smaller and one for the larger angle.

and co-workers.^[37,38] In the *trans*→*cis* photoisomerization, a modest repopulation of the S_2 state occurs in the $\angle \text{CNNC} \cong 90^\circ$ region, where the S_2 PES has a minimum rather close to S_1 . In the *cis*→*trans* case about 15% of the trajectories remain in S_2 when travelling from $\angle \text{CNNC} \cong 0^\circ$ to 90° . In both cases we have verified that the more or less prolonged transit on the S_2 PES does not influence the quantum yields significantly: in fact, distinct subsets of trajectories, found or not found in S_2 at a given torsion angle, contain approximately the same fraction of reactive and unreactive trajectories.

The S_1 state in turn decays to S_0 almost completely within 1 ps, when starting from TAB, and much faster (about 300 fs) when starting from CAB. This is true both with $\pi \rightarrow \pi^*$ and with $n \rightarrow \pi^*$ excitation, and is in agreement with the shorter lifetimes assigned to *cis* S_1 by time-resolved investigations (see Table 6). Moreover, a recent determination of the fluorescence quantum yields^[40] assigns a value of 0.3 to the lifetime ratio $\tau_{\text{cis}}/\tau_{\text{trans}}$. As already anticipated, an important fraction of the trajectories land on the ground state too early, that is, before the CNNC angle has gone beyond 90° : in this way, the slope of the S_0 PES tends to bring the molecule back to the starting isomer. In Table 4 we have listed

$\langle \theta \rangle$, that is the average CNNC angle, at the time of the first and last surface hopping from S_1 to S_0 (notice that several hops may take place between these two states for each trajectory). In all cases, at the time of the first hop, $\langle \theta \rangle$ is still short of the 90° midpoint value (i.e., $\langle \theta \rangle < 90^\circ$ when starting from CAB and $\langle \theta \rangle > 90^\circ$ when starting from TAB). However, the angular velocity $\langle d\theta/dt \rangle$ for the reactive trajectories has the right sign to bring the molecule beyond the barrier in the ground state, thanks to the inertia of the torsional motion: $\langle d\theta/dt \rangle$ is negative when starting from TAB, and positive when starting from CAB. In fact, at the time of the last hop the dihedral angle has moved closer or even beyond 90° . For the unreactive trajectories the values of $\langle \theta \rangle$ and $\langle d\theta/dt \rangle$ are invariably less favourable: namely, in all four cases the sign of $\langle d\theta/dt \rangle$ at the last hop time is opposite to that of the reactive trajectories.

Having established that the quantum yields are determined by the balance between the contrasting effects of early IC and torsional inertia, we can examine how the initial excited state influences such effects. Upon $\pi \rightarrow \pi^*$ excitation, we find that the majority of the trajectories start in S_2 , since the $S_0 \rightarrow S_3$ transition has a smaller oscillator strength. Figure 5 shows that the lifetime of S_2 is about 100 fs. At the

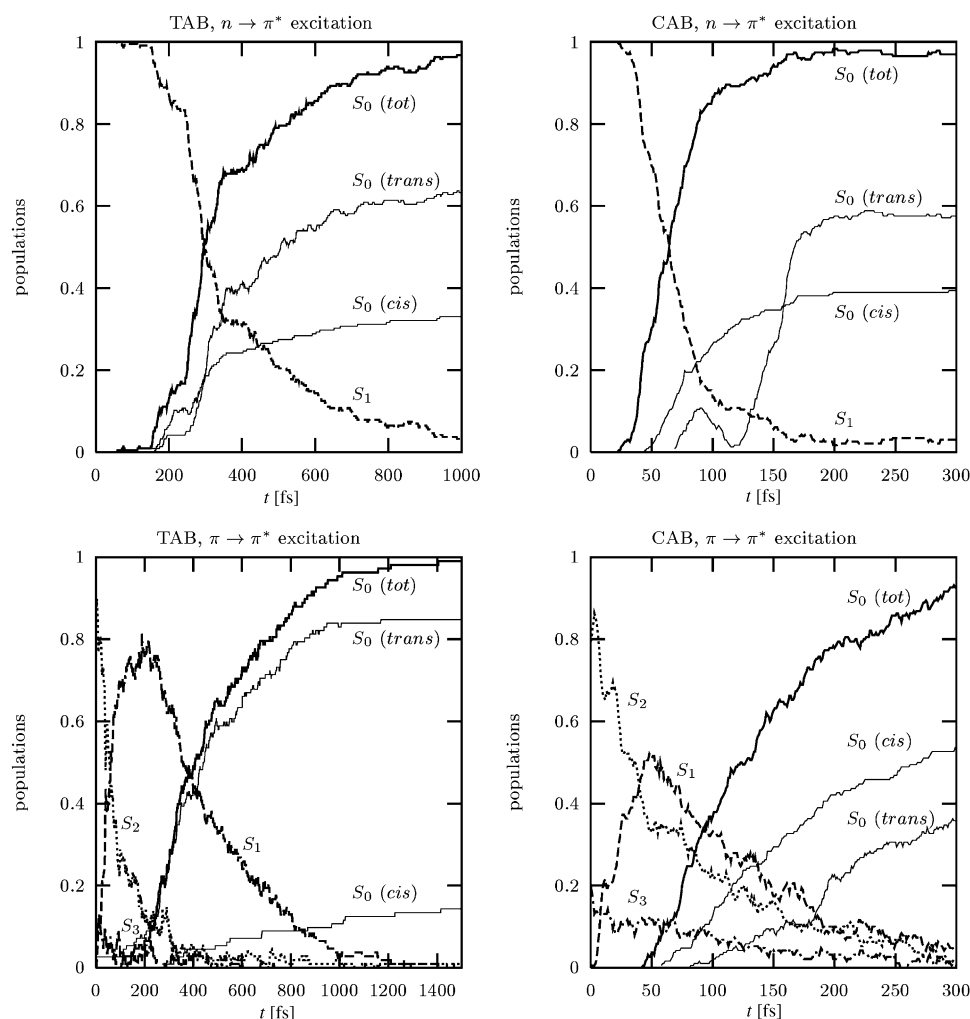


Figure 5. Time-dependent populations of the electronic states.

time of the first $S_2 \rightarrow S_1$ hop the average CNNC angle has made almost no progress with respect to the transoid initial conditions (see Table 4), while, starting from CAB, it has changed by about 18° only. The further decay to S_0 occurs somewhat later than in the case of direct excitation to S_1 . For the unreactive trajectories, the $S_1 \rightarrow S_0$ IC is delayed by 50–80 fs, which is less than the lifetime of S_2 . The $\langle \chi \rangle_{\text{CNNC}}$ averages and related angular velocities are less favourable to the accomplishment of isomerization than with $n \rightarrow \pi^*$ excitation. In conclusion, with more vibrational energy the decay of S_1 is slightly faster, but the torsion around the double bond is not.

The reason is that the crossing seam between S_0 and S_1 is reached more easily, and with values of the torsion angle further from 90° , if more energy is available. As already noted, the crossing seam coincides with the minimum energy path in S_1 only in its lowest part, between $\langle \chi \rangle_{\text{CNNC}} \cong 80^\circ$ and $\langle \chi \rangle_{\text{CNNC}} \cong 105^\circ$ (see Figure 2). For CNNC angles outside this range, a variable amount of vibrational energy is needed in the suitable internal modes. To show how the dynamics following $n \rightarrow \pi^*$ and $\pi \rightarrow \pi^*$ excitation differ under this respect, we plot in Figure 6 the S_0 and S_1 potential energies U_K as functions of the torsion angle, averaged over all trajectories. The S_0 – S_1 energy gap of

course reduces progressively as $\langle \chi \rangle_{\text{CNNC}}$ approaches 90° , with either $n \rightarrow \pi^*$ or $\pi \rightarrow \pi^*$ initial excitation. Notice that the two average energies $\langle U_K \rangle$ never cross, since by definition $U_1 \geq U_0$ even when the two electronic states actually swap. In order to compare the probability of getting close to the crossing seam in the different cases, we have also represented the standard deviations σ_K of the averages $\langle U_K \rangle$. We find that both σ_0 and σ_1 are larger in the case of $\pi \rightarrow \pi^*$ excitation, because more vibrational energy is available. We shall assume that the condition $\langle U_1 \rangle - \sigma_1 = \langle U_0 \rangle + \sigma_0$ results in approximately the same, non-negligible, probability of approaching the crossing seam for all cases. The plots indicate that, with $\pi \rightarrow \pi^*$ excitation, the above condition is reached for torsion angles substantially closer to the starting one, in comparison with the $n \rightarrow \pi^*$ case. As a consequence, “earlier” decay occurs and the quantum yield is lowered.

The optimized geometries of the S_0 – S_1 crossing seam (see Figure 1 and Table 3) and the average $\langle \chi \rangle_{\text{CNNC}}$ values at the time of the $S_1 \rightarrow S_0$ surface hoppings (Table 4) suggest that the most effective internal mode in promoting the IC is the symmetric opening of the NNC angles. This is particularly clear in the case of $\text{trans} \rightarrow \text{cis}$ photoisomerization, where the dependence of the quantum yield on the initial excited state is sharper. In fact, the IC to S_0 occurs when the $\langle \chi \rangle_{\text{CNNC}}$ averages are between 132 and 139° with $n \rightarrow \pi^*$ excitation, and 134 – 140° with $\pi \rightarrow \pi^*$ excitation: in both cases the NNC angles are larger than in the minimum of the S_1 PES. To reach the energy minimum of the conical intersection, which practically coincides with the S_1 PES minimum, it would not be necessary to open the NNC angles so much: however, this deformation allows the molecule to approach the crossing seam earlier, at CNNC angles considerably different from 90° (see Figure 1 and Table 3), so favouring the early IC. The location of the S_2 – S_1 conical intersection, with $\langle \chi \rangle_{\text{CNNC}}$ about 5° smaller than in the S_0 and S_2 minima, brings about a higher degree of vibrational excitation for the NNC symmetric bending mode, than in the case of direct excitation to S_1 . So the photoisomerization dynamics and the quantum yields are strongly influenced by the electronic structure of the excited states, which determines the shape of the PES. Quite clearly this description of the nonadiabatic dynamics incorporates the gist of Diau’s propos-

Table 6. Pump-and-probe and other time-resolved experiments performed on *trans*- and *cis*-azobenzene. Excitation and transient absorption wavelengths (λ) and transient lifetimes (τ).

<i>trans</i> -azobenzene reference	λ (pump) [nm]	λ (probe) [nm]	τ [ps]
Lednev et al. ^[32]	303	370–450, max at 390	0.9–1.2, 13
Lednev et al. ^[33]	280	390–420	0.8, 14
	300	max at 475	< 0.18
	300	max at 400	0.8, 10
Fujino and Tahara ^[36]	273	Raman ^[a]	1, 16 ^[b]
Fujino et al. ^[37]	280	fluor. S_2 ^[c]	≈ 0.1
	280	fluor. S_1 ^[d]	≈ 0.5
Fujino et al. ^[38]	267	max at 475, 600	< 0.5
	267	max at 410, 500	0.9, 17
Schultz et al. ^[41]	330	207 ^[e]	0.17, 0.42
Lednev et al. ^[33]	390, 420	360–420, 500–700	0.6, 2.6
	445	max at 400, 550	2.3
Nägele et al. ^[34]	435	459, 563	0.32, 2.1
Lu et al. ^[39]	432	fluor. S_1 ^[d]	0.16–0.28, 0.78–1.56 ^[f]
Satzger et al. ^[40]	480	370–580, max at ~ 400 , 530	0.35, 3
		max at < 370	12
<i>cis</i> -Azobenzene reference	λ (pump) [nm]	λ (probe) [nm]	τ [ps]
Hamm et al. ^[35]	408	IR ^[g]	≈ 20
Nägele et al. ^[34]	435	max at 360	0.18, 2, 20
	435	max at 550	0.18, 2, 10
Satzger et al. ^[40]	480	370–630, max at 540	0.1, 0.9
		max at < 370	5.6

[a] Raman spectrum based on the 410 nm absorption band. [b] Obtained in hexane; in ethylene glycol, a single lifetime of ≈ 12.5 is observed. [c] Upconverted fluorescence band at 380–480 nm. [d] Up-converted fluorescence band at 550–750 nm. [e] Time-resolved photoelectron spectroscopy. [f] τ increasing with fluorescence wavelength. [g] Infrared frequencies around 1500 cm^{-1} .

al,^[29] that the symmetric NNC bending mode would contribute to the deactivation of S_1 ; however, the S_1 – S_0 transitions actually take place at geometries with some degree of torsion ($\angle \text{CNNC} = 90$ – 160° , on the *trans* side) rather than along a pure double inversion pathway.

Figure 7 is a sketch of the first three PES, showing two typical trajectories, one starting in S_1 and the other in S_2 . It offers a simplified view of the reaction mechanism, which can be summarized as follows (the first two steps apply only to $\pi \rightarrow \pi^*$ excitation):

- 1) excitation to S_2 (or to S_3 with ultrafast decay to S_2);
- 2) closing of the NNC angles to reach the S_1 – S_2 crossing seam, using some of the extra vibrational energy available after excitation (actually the optimized conical intersection lies lower than the Franck-Condon point);
- 3) torsion (decrease of CNNC towards 90°) and wide oscillations of the NNC coordinate, in the S_1 surface;
- 4) approach to the S_0 – S_1 crossing seam, possibly with rather large values of NNC, and CNNC still in the neighborhood of 130° ;
- 5) decay to S_0 and, most of the times, reversion to the initial isomer, TAB (this part of the trajectory is not shown in the figure).

The direct excitation to S_1 qualitatively follows the same steps 3 to 5, but with a smaller amplitude of the NNC oscillations, determined by the difference in the S_0 and S_1 equilibrium angles. As a consequence the S_0 – S_1 crossing seam is hit with smaller NNC and with CNNC closer to 90° , so in-

creasing the probability of isomerization. It is important to note that, although the NNC bending oscillations are more pronounced after $\pi \rightarrow \pi^*$ than after $n \rightarrow \pi^*$ excitation, their experimental detection will be easier in the latter case: in fact, the S_2 – S_1 decay, taking place in a time comparable with the symmetric NNC bending vibrational period, destroys the coherence of the wavepacket (see Figure 4).

Time-Dependent Spectroscopy

Table 6 summarizes the results of time-resolved spectroscopic experiments. Transients have been monitored by IR and UV/Vis absorption, Raman, and fluorescence spectroscopy. The $\pi \rightarrow \pi^*$ excitation of TAB yields transients with lifetimes of three distinct orders of magnitude: 0.1–0.5, 0.8–1.2, and 10–

16 ps, respectively. Approximately the same lifetimes (0.2, 2, 10–20 ps) were also observed after $n \rightarrow \pi^*$ excitation of CAB, and the two shorter ranges (0.16–0.6, 0.8–2.6) also by $n \rightarrow \pi^*$ excitation of TAB. No experiments concerning the $\pi \rightarrow \pi^*$ photolysis of CAB have been performed to our knowledge. In interpreting such results, one should take into account the motion of the wavepacket on the PES, that is, the geometrical relaxation of the molecule, which brings about changes in position, shape and intensity of the absorption/emission bands. Therefore, a transient lifetime obtained at a fixed probe wavelength cannot be simply assumed to correspond to the lifetime of an excited electronic state. This is one of the reasons why different times have been measured, even in similar excitation conditions.

We have simulated the transient absorption and emission spectra which can be expected in each of the four basic experiments ($n \rightarrow \pi^*$ or $\pi \rightarrow \pi^*$ excitation of TAB or CAB), as described in Appendix C. In fact, the simulated emission spectra are more complete and reliable than the absorption ones, first of all because photon absorption may end up in states higher than S_3 , not considered in this work. Moreover, the absorption transients are measured as difference spectra, with respect to the equilibrium (pre-excitation) condition. Of course, the subtraction operation mainly affects the region with $\lambda < 360$ nm ($\pi \rightarrow \pi^*$ band) and is quite irrelevant for $\lambda > 500$ nm, where both TAB and CAB are transparent. The absorption from hot S_0 , produced by IC from higher states, can differ substantially from that of thermally equilibrated S_0 , especially in the case of the forbidden $n \rightarrow \pi^*$ band of TAB. The strongest S_0 absorption is anyway due to

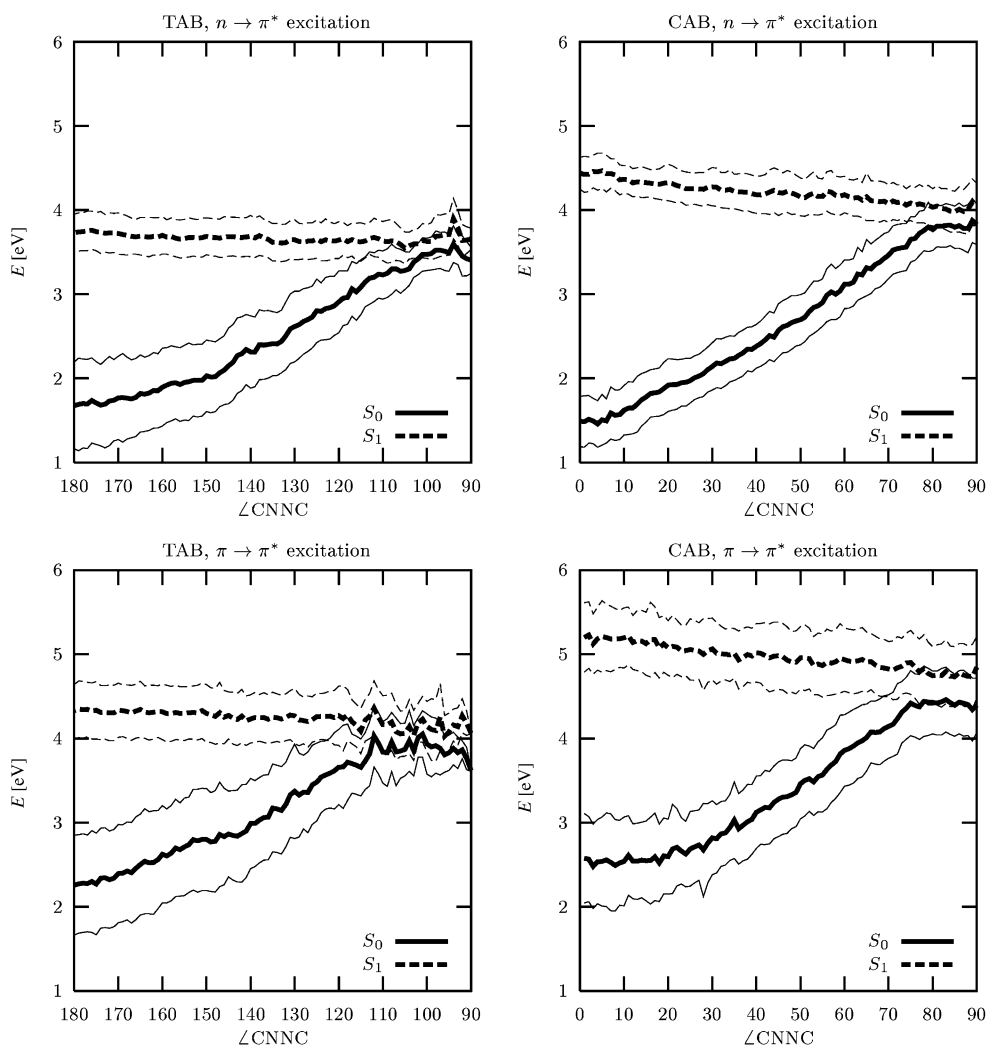


Figure 6. Average S_0 and S_1 potential energies (thick lines) \pm standard deviations (thin lines), as functions of the leading coordinate $\angle\text{CNNC}$.

the $\pi \rightarrow \pi^*$ band, and has been detected by Lednev et al.,^[32,33] Nägele et al.^[34] and Satzger et al.^[40] in the 360–450 nm range, red shifted with respect to the normal spectrum. While we confirm qualitatively the position of these bands, we cannot presently simulate them adequately, because we should prolong our trajectories in the S_0 PES instead of stopping them after isomerization. Moreover, the transient decays are in this case rather complex, with lifetimes spanning almost two orders of magnitude. The shorter ones are probably due to the motion of the wavepacket (mainly torsion) and to internal vibrational relaxation (energy transfer from torsion and a few other modes which are initially excited, to all other modes). The longer lifetimes (10–20 ps) correspond to energy transfer to the solvent: these values compare well with our previous findings for the photolysis of azomethane in water solution,^[45] but could not have been found in the present isolated molecule study, even prolonging the simulations in time. Hot ground state was also detected by the IR and Raman measurements of Hamm et al.^[35] and Fujino and Tahara,^[36,38] and solvent relaxation was monitored by Terazima et al.^[46] in all cases, the same long lifetimes were found.

The only part of the transient absorption spectra we can reproduce at least semiquantitatively is the $S_1 \rightarrow S_{2,3}$ band which takes place at $\lambda > 400$ nm. This is illustrated in Figure 8. As already observed, transitions from S_1 to S_4 or higher states, not taken into account in our simulation, may contribute to the transient spectrum at shorter wavelengths. The $n \rightarrow \pi^*$ excitation of both TAB and CAB yields the bands observed by Lednev et al.,^[33] Nägele et al.^[34] and Satzger et al.^[40] at 500–700 nm. Both the $S_1 \rightarrow S_2$ and the $S_1 \rightarrow S_3$ transitions are active and in CAB they can be distinguished (see for comparison refs. [34,40]). However, our transient spectra can be fitted with good accuracy by a single exponential, with lifetimes $\tau_1 = 350$ fs for TAB and 50 fs for CAB. To explain the presence of the weaker components with longer lifetime, found in the quoted experiments, one could invoke a contribution of ground state absorption also at these wavelengths, or a slowing down effect due to the solvent, which is absent in our simulations. Another possibility is a specific failure of the semiclassical model: quantum mechanical full multiple spawning calculations^[47] are in progress to bring out such a possibility.

By $\pi \rightarrow \pi^*$ excitation of TAB, we find a signal $X(t)$ with a clear biexponential behaviour, due to the consecutive decay

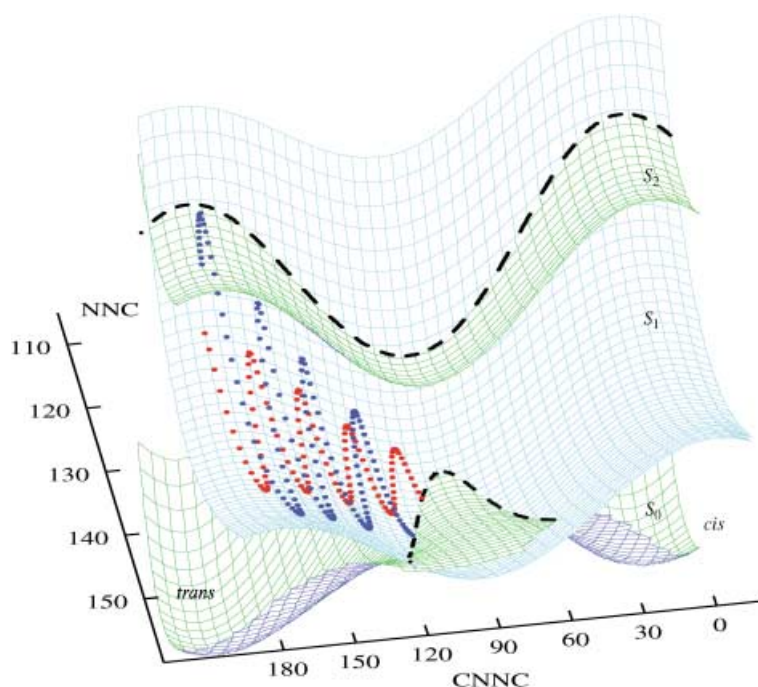


Figure 7. Sketchy view of the S_0 , S_1 and S_2 PES, as functions of the torsional angle CNNC and of the symmetric NNC bending coordinate. Dashed lines indicate the crossing seams. Two typical trajectories are shown, one starting in S_1 (red dots) and the other one in S_2 (blue dots).

law $X(t) \propto \exp(-t/\tau_1) - \exp(-t/\tau_2)$, where τ_1 and τ_2 are the lifetimes of S_1 and the pair S_2 – S_3 , respectively. This simple situation is due to the good separation of the time scales ($\tau_1 \gg \tau_2$), while the S_2 – S_3 population exchange is even faster. If we take $\tau_2 = 130$ fs, from the decay of the corresponding fluorescence band (see below), the fit of the $S_1 \rightarrow S_n$ absorption band yields $\tau_1 = 400$ fs. This is only slightly longer than by direct $n \rightarrow \pi^*$ excitation, and is, again, in agreement with the short lifetime components of the experimental spectra. For CAB we cannot do the same analysis, because both lifetimes are very short and of the same order of magnitude, about 100 fs (see also Figure 5).

The simulated time-resolved fluorescence spectra do not suffer from the same drawbacks as the absorption ones. They are shown in Figure 9. Experiments were done only with TAB. Lu et al.^[39] measured the up-converted fluorescence after $n \rightarrow \pi^*$ excitation and interpreted their results according to the rotation mechanism of photoisomerization. They found a two-component decay, with lifetimes depending on the emission wavelength, in the ranges 160–280 fs and 780–1560 fs. We only find $\tau_1 = 190$ –306 fs, which increases as the wavelength goes from 580 to 760 nm; this is in agreement with the short lived component of Lu et al. If we compare the emission and absorption lifetimes, derived both from measurements^[39,34] and from simulations, we see that fluorescence decays faster than absorption. Both features, that is, fluorescence lifetimes increasing with wavelength, and shorter than those of absorption from the same state, are due to the motion of the excited state wavepacket. In fact, the long wavelength emission is generated at longer delay times after excitation, when the wavepacket samples

lower portions of the S_1 PES, corresponding to smaller S_1 – S_0 energy gaps. On the other hand, for the same reason, the ΔE^3 dependence of the spontaneous emission rates accelerates the decay of the fluorescence with respect to that of absorption, because at later times the average ΔE is smaller. These rather subtle effects illustrate well the general caveat against identifying the lifetimes of spectroscopic transients with those of electronic states. As already noted, in the simulated fluorescence spectra as in the absorption ones we lack the slow decaying (1–2 ps) component. Of the two explanations put forward in discussing the absorption transients, only the effect of solvent friction can be invoked in the case of fluorescence. The fluorescence decay of $n \rightarrow \pi^*$ excited CAB is much faster than that of TAB (≈ 50 fs), with a maximum in-

tensity at 400 nm: no measurements are available in this case.

The transient fluorescence of TAB after $\pi \rightarrow \pi^*$ excitation has been detected and accurately analyzed by Fujino et al.^[37,38] Our results are in good agreement with theirs. A strong band at short wavelengths is due to $S_2 \rightarrow S_0$ emission, with a small contribution of $S_3 \rightarrow S_0$, and decays with a lifetime $\tau_2 = 130$ fs. Another weak band in the 500–900 nm interval is due mainly to S_1 emission, superimposed to the queue of the $S_{2,3}$ band ($S_{2,3} \rightarrow S_1$). We tried to fit the time dependence by the consecutive decay law $X(t) \propto \exp(-t/\tau_1) - \exp(-t/\tau_2)$, assuming $\tau_2 = 130$ fs, as we did for the S_1 absorption spectrum. The resulting τ_1 varied from 220 to 360 fs according to the wavelength, mainly because of the variable contribution of the fast S_2 component. By taking the pure S_1 component, as Fujino et al did by decomposition of the time-dependent signal, we get $\tau_1 = 410$ fs at 600 nm, in good agreement with their result (500 fs). The $\pi \rightarrow \pi^*$ excited CAB fluorescence spectrum is more complicated, in that the S_2 and S_3 emissions give place to separate bands, so one can see a three-step consecutive decay, but with very short lifetimes, as already noted when commenting the absorption results.

A special place should be reserved to the time-resolved photoelectron spectra measured by Schultz et al.^[41] upon excitation of TAB with $\lambda = 330$ nm. This is the only published experimental study conducted in a molecular beam, rather than in solution. In the interpretation of the authors, these measurements reveal the existence of a fourth excited state, S_4 , associated with a peak centred at 0.15 eV in the photoelectron energy spectrum. In fact, the vertical excitation energy to S_4 , according to CASSCF, CASPT2 and TD-DFT

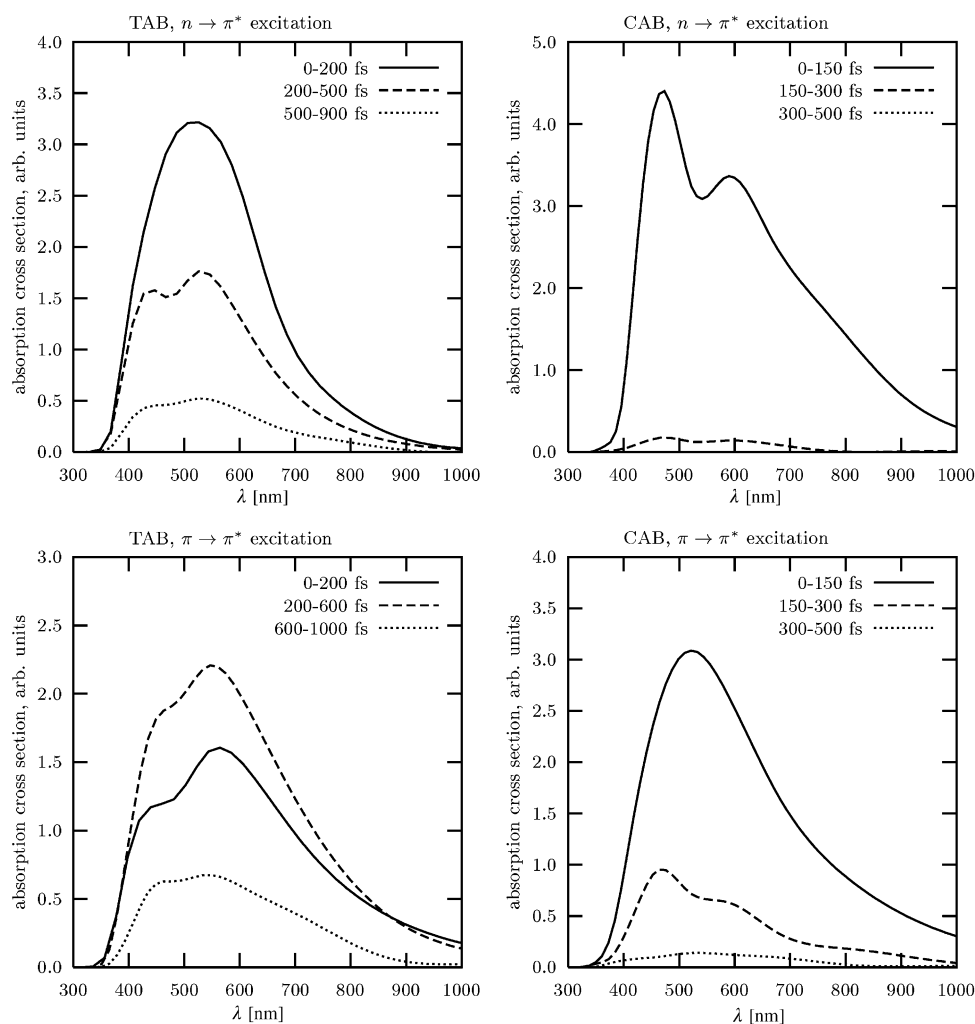


Figure 8. Simulated transient absorption spectra, averaged over three different time intervals. Only the $S_1 \rightarrow S_{2,3}$ transition is shown.

calculations by the same authors, is very close to that of S_2 and S_3 . It gives place to an allowed transition, whereas $S_0 \rightarrow S_3$ is forbidden: this is why Schultz et al. emphasize the importance of S_4 relative to S_3 , although also the computed $S_0 \rightarrow S_4$ oscillator strength is much smaller than that of S_2 . Since they find a lifetime of 420 fs for the associated transient, they propose that populating this relatively long lived state makes the difference between the $n \rightarrow \pi^*$ and the $\pi \rightarrow \pi^*$ photochemistry. We did not include S_4 in our calculations, but our S_3 state is initially populated at least as much as the computed oscillator strength of S_4 would imply: this may happen because at distorted geometries the transition to the genuine S_3 (1A_g) state is no longer forbidden, and/or because the S_3 and S_4 energies actually swap according to the geometry. In any case, it seems unlikely that the upper state of a very close lying pair should live for 420 fs, and we find that S_3 itself decays in about 100 fs, together with S_2 , in agreement with Fujino et al. experiments.^[37,38] Another plausible assignment for the 0.15 eV band in the photoelectron spectrum is the transition from S_1 to the first or second ionic state^[48] (D_0 or D_1), that should be observed approximately

at the same energy as the $S_{3,4} \rightarrow D_{2,3}$ transition postulated by Schultz et al. However, the $S_1 \rightarrow D_{0,1}$ band should appear with a time delay due to the lifetime of S_2 , whereas no delay is detected experimentally. On the basis of the above considerations, we propose that both the $S_{3,4} \rightarrow D_{2,3}$ and $S_1 \rightarrow D_{0,1}$ transitions contribute to the 0.15 eV band at short and at long times, respectively; the 420 fs lifetime would then be essentially that of S_1 , in agreement with other experimental determinations and with our simulations. Schultz et al. also observe another band, corresponding to a photoelectron energy of 1.15 eV, with a lifetime of 170 fs: in this case we agree with them in attributing it to the $S_2 \rightarrow D_0$ transition.

Concluding Remarks

The mechanism of photochemical reactions is quite a difficult subject, which is most appropriately tackled by a combined theoretical and experimental approach. Single experiments, in the absence of a firm theoretical basis, can be interpreted in many different ways. Computational simulations, only recently

become available for molecules as large as azobenzene, can be questioned mainly as to the accuracy of the PES on which they are based. The semiempirical PES presented in this work are more accurate than the ab initio ones currently used for this kind of studies.

The present investigation of azobenzene photoisomerization highlights the above considerations. In the lack of a solid theoretical background, for at least two decades the difference in the quantum yields obtained with $n \rightarrow \pi^*$ and $\pi \rightarrow \pi^*$ photolysis has been attributed to the existence of two distinct isomerization pathways, inversion and torsion. Our simulations show that only one mechanism operates, namely torsion of the N=N double bond. The inversion pathway in the S_1 PES is not energetically forbidden, but is much less favourable: in fact, preliminary results^[19] on the photoisomerization of azabenzophenones^[21,25,26] show that inversion can play a role in the presence of conformational constraints. Of course further refinements of the PES may change in the future some details of our results, but we think that the main features are correct, first of all because of the good agreement with nearly all experimental findings.

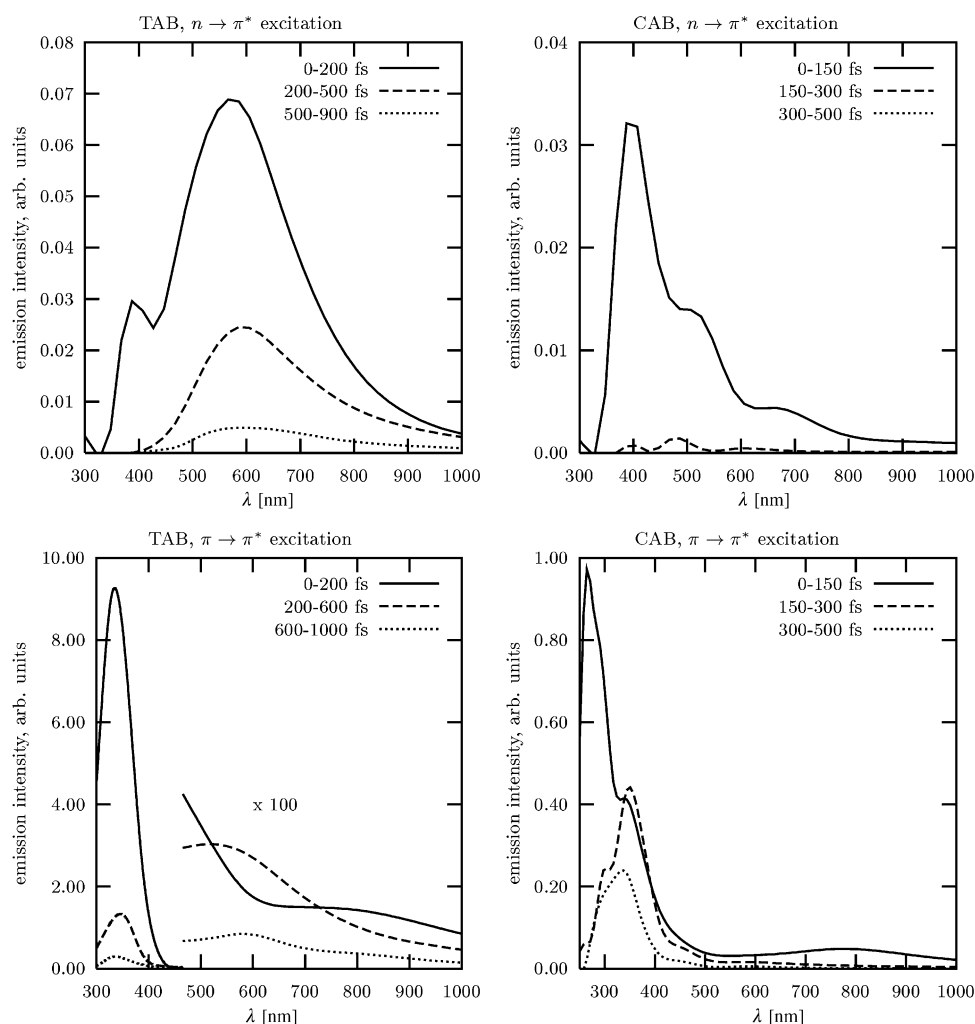


Figure 9. Simulated transient emission spectra, averaged over three different time intervals.

We have demonstrated that rather subtle changes in the coupled nuclear and electronic dynamics can explain the violation of Kasha's rule. The case of azobenzene photoisomerization, as we understand it now, illustrates the respective roles of the inertia of nuclear motion along the reaction coordinate and of the nonadiabatic transitions between electronic states, which may have opposite effects on the quantum yields of any reversible photoisomerization $A \rightleftharpoons B$. When all molecules, both in the direct and in the inverse reaction, go through a common intermediate C in the excited state, with a lifetime long enough as to lose the memory of the starting isomer, the sum of quantum yields $\Phi_{A \rightarrow B} + \Phi_{B \rightarrow A}$ must be one. The competition of nonadiabatic and/or radiative decay processes acting before C is reached ("early deactivation") will lower the quantum yields ($\Phi_{A \rightarrow B} + \Phi_{B \rightarrow A} < 1$). On the other hand, if C is a very efficient funnel, the nuclear momentum gained during the $A \rightarrow C$ or $B \rightarrow C$ geometrical relaxation will not be lost completely before reverting to the ground state ("memory effect"), thus increasing the reaction probability in both directions: in this case one might even find $\Phi_{A \rightarrow B} + \Phi_{B \rightarrow A} > 1$. But in fact the memory effect, since it requires very efficient nonadiabatic couplings,

will hardly occur without the adverse influence of early deactivation. That of azobenzene is probably a typical example of ultrafast photoisomerization, where both effects are important. The difference between $n \rightarrow \pi^*$ and $\pi \rightarrow \pi^*$ excitation consists in details of the wavepacket dynamics in the S_1 PES: it is mainly the larger amplitude of the symmetric NNC bending motion that shifts the balance toward early deactivation in the $\pi \rightarrow \pi^*$ case.

In the last years, a variety of time resolved spectroscopic techniques have been applied to the study of azobenzene photoisomerization. While none of these experiments, taken alone, can yield the key for the solution of the mechanistic problem, they are a source of hard data which must find an explanation in the framework of the proposed mechanism, as shown in the preceding section. We generally find a good agreement between our simulated spectra and the observed transients. In order to account for medium and long lifetime components of the spectra (1–10 ps), we shall need to run simulations of the photoisomerization in a solvent cluster,

which is now possible by means of the QM/MM extension of our technique.^[17,18] Further experiments may confirm the gist of our results. In particular, we predict that the $n \rightarrow \pi^*$ excitation of *trans*-azobenzene is followed by oscillations in the symmetric NNC bending mode, rather than in the asymmetric one which would prelude to N-inversion. The excitation of this important vibrational mode might be detected by resonant Raman spectroscopy, thus settling the question of inversion versus rotation mechanism in the S_1 state. We have also formulated predictions for the fluorescence and absorption transient spectra of $\pi \rightarrow \pi^*$ excited *cis*-azobenzene, which have not yet been observed.

Appendix A: Optimization of Semiempirical Parameters

The optimization of the semiempirical parameters took as a starting point the standard AM1.^[49] No changes were made for the H atoms. The C atom parameters had already been optimized for the benzene molecule, taking into account seven electronic states; the optimization aimed at reproducing high quality ab initio data for planar and distorted equilibrium geometries, transition energies and conical intersection points.^[50]

Only the N atom parameters were modified in view of adjusting the first four singlet PES of azobenzene to reproduce the available ab initio^[27] and experimental data. The target values we considered for the re-parametrization are listed in Table 1; they were mainly energy differences, with the addition of some geometry data concerning equilibrium structures. We soon discovered that AM1, however re-parametrized, yields too large equilibrium values for the NNC angles and a too low inversion barrier in the ground state. Therefore we added a correction to all the PES, in the form:

$$U_{\text{corr}}(\theta_1, \theta_2) = \frac{P_1 + \cos(2\phi)}{P_1 + 1} \sum_{i=1}^2 P_2 \left[\cos\left(\pi \frac{\theta_i - P_3}{\pi - P_3}\right) + 1 \right] \quad (1)$$

where θ_1 and θ_2 are the two NNC angles and $\phi = \angle \text{CNNC}$. P_1 , P_2 and P_3 are adjustable parameters which were optimized along with all other semiempirical parameters.

The optimization is done by searching for minima of the weighted sum of square errors:

$$F(\mathbf{P}) = \left[\sum_i \left(\frac{V_{\text{si}}(\mathbf{P}) - V_{\text{ti}}}{V_{\text{ti}}} \right)^2 W_i \right] \left[\sum_i W_i \right]^{-1} \quad (2)$$

where V_{ti} are the energetic and geometrical data to be reproduced (target values), and V_{si} their semiempirically computed counterparts, which depend on the parameter set \mathbf{P} ; the W_i are weights. Fifteen parameters were optimized, that is, the whole AM1 set, with the exclusion of the Slater exponent of the basis functions, and with the addition of P_1 , P_2 and P_3 (see above).

The geometries of both stable isomers were taken from X-ray diffraction studies.^[51,52] The orientation of the phenyl groups in TAB is an object of controversy. Earlier electron diffraction measurements^[53] were interpreted in favour of a substantial non-planarity (NNCC angles of about 30°), while a more recent study by Tsuji et al.,^[54] taking explicitly into account the torsional potential, finds a shallow minimum at $\angle \text{NNCC} = 0^\circ$ (C_{2h} symmetry), with torsional barriers of less than 2 kcal mol⁻¹. SCF, DFT and MP2 calculations^[54–56] gave different results, mostly in favour of a planar structure. The coupling between the two torsions is weak,^[54] therefore the C_1 and C_2 structures with the same NNCC angles have almost equal energies. Given the uncertainty of these results, we have not included them in the target function, and we have a posteriori verified that the torsional potential is very flat at within the first 20°. Experimentally the *cis*–*trans* energy difference in the ground state is 9.9–12 kcal mol⁻¹ and the best theoretical calculations yield slightly higher values,^[27,56,57] therefore we have set the target value of 12 kcal mol⁻¹.

The vertical transition energies are normally thought to correspond to maxima in the absorption spectra.^[33,34,37] In the case of azobenzene, our ab initio calculations^[27] showed that S_2 and S_3 are very close in energy; moreover, in TAB the 1A_g state (S_3) gives place to a forbidden transition, which is probably not detectable in the spectrum. Therefore, we have assumed the same target values for the vertical transition energies of S_2 and S_3 (see Table 1). We implicitly neglect the zero-point energy, which is consistent with the use we shall make of the semiempirical PES, in the semiclassical simulations. The ground and excited state energies for the rotamer (ROT), the perpendicular invertomer (PER) and the planar invertomer (PLA) shown in Figure 1, have been taken from our previous ab initio calculations.^[27]

The minimization was performed by means of the simplex method, combined with simulated annealing.^[58] Table 1 shows both the target values V_{ti} and the semiempirically computed ones, V_{si} .

Appendix B: New Procedure for Conical Intersection Optimization

The potential energy U_K of an excited state can be optimized with respect to the internal coordinates, with the constraint of degeneracy with another

state L ($U_K = U_L$). In this way, one finds the minimum energy conical intersection point for states K and L . Algorithms that locate the crossing seam and simultaneously minimize the potential energy have been put forward in the past years^[59–62] and have also been applied in conjunction with our semiempirical method.^[63] All these methods require the calculation of derivative couplings, that are not implemented for all kinds of wave functions and in all computational packages. Moreover, the optimization of conical intersections often runs into problems because very distorted geometries are reached: this depends on a delicate balance between the two goals of the search algorithm (approaching the crossing seam and minimizing the energy), which is influenced by the starting point as well as by operative options. Therefore we have implemented another method for crossing seam optimization, of comparable efficiency and to be used as an alternative to the existing ones. The new method does not require the calculation of derivative couplings and can be applied also to crossings between states of different spin symmetry.

The new algorithm is based on a penalty function. We use the standard optimizers (for instance BFGS as implemented in MOPAC^[42]), to search the space of the nuclear coordinates \mathbf{Q} for the minimum of a modified potential energy function $F(\mathbf{Q})$. The function F contains two terms: one is the average of the state energies and the other one is a penalty function, monotonously increasing with the energy difference $\Delta U = U_K - U_L$. We have

$$F(\mathbf{Q}) = \frac{U_K + U_L}{2} + \alpha \beta^2 \ln \left[1 + \left(\frac{U_K - U_L}{\beta} \right)^2 \right] \quad (3)$$

where α and β are suitable constant parameters. The penalty function (second term in the r.h.s.) forces the optimization to approach the crossing seam, without altering the position of the minimum. In fact, for $\Delta U \ll \beta$ the function is quadratic in ΔU : $F \approx (U_K + U_L)/2 + \alpha \Delta U^2$. Therefore, the larger is α , the closer to the crossing seam is the minimum of $F(\mathbf{Q})$. For $\Delta U \gg \beta$ the penalty function is proportional to $\ln(\Delta U)$, so it does not force a too fast approach to the crossing seam, which might result in a large increase of the average energy, corresponding to highly distorted geometries. Reasonable parameter values are of the order of $\alpha = 5$ (kcal mol⁻¹)⁻¹ and $\beta = 5$ (kcal mol⁻¹).

Appendix C: Initial conditions and Simulated Spectra

The initial conditions for a swarm of trajectories are sampled according to the following prescriptions. First a Brownian trajectory is run in the ground state, starting from the minimum corresponding to one of the stable isomers, with $T = 298$ K. The Brownian motion is generated by integrating Langevin's equations^[64] for a time (8 ps) long enough as to warrant an adequate sampling of the largest amplitude motions, namely the rotation of the phenyl rings. The Brownian trajectory provides a number of points in the phase space of the nuclear coordinates and momenta, distributed according to Boltzmann's statistics. For each point we calculate the excitation energies $\Delta E_K = U_K - U_0$ (U_K being the electronic energy of state K) and, for each ΔE_K falling in the required range, we evaluate the excitation probability, proportional to the square transition dipole $|\langle 0 | \vec{\mu} | K \rangle|^2$. A stochastic algorithm generates zero, one or more vertical excitations to each state K for the current phase space point, according to the computed probability. Each excitation gives place to one trajectory: notice that, because of the surface hopping stochastic algorithm, trajectories starting with the same initial conditions will be generally different. The procedure generates, as a by-product, a distribution of excitation energies, that is, a simulated absorption spectrum for the ground state at thermal equilibrium.

Time-resolved absorption and emission spectra for the excited molecule can be generated from the nonadiabatic trajectory results, by the following procedure. For each time step within a given interval (t_b , t_e), we sum the contributions due to all trajectories to the absorption probability P_A and to the emission probability P_E . For each trajectory, we consider the current PES U_K and we calculate the transition energies $\Delta E = U_L - U_K$ ($L > K$) and the relative contributions to P_A , proportional to μ_{KL}^2 .

(square transition dipole). The function $P_A(\Delta E)$ is then generated in the form of a histogram and normalized both with respect to the number of trajectories and to the time interval ($t_{\text{tr}} t_c$). In the same way we construct the emission spectrum $P_E(\Delta E)$, by considering transitions $K \rightarrow L$ with $L < K$ and contributions proportional to $\mu_{\text{KL}}^2 (U_K - U_L)^3$. Notice that, because of the truncation of the basis of electronic states, the simulated absorption spectrum is not complete, especially in the short wavelength region.

Acknowledgement

We are grateful to E. W.-G. Diau, T. J. Martínez, G. Orlandi, A. Stolow, T. Tahara and J. Wachtveitl, for enlightening discussions and for communicating to us their results prior to publication. This work was supported by grants of the Italian M.I.U.R. and of the University of Pisa.

- [1] T. Ikeda, O. Tsutsumi, *Science* **1995**, 268, 1873.
- [2] I. Willner, S. Rubin, A. Riklin, *J. Am. Chem. Soc.* **1991**, 113, 3321.
- [3] V. Balzani, A. Credi, M. Venturi, *Coord. Chem. Rev.* **1998**, 171, 3.
- [4] M. S. Vollmer, T. D. Clark, C. Steinem, M. Reza Ghadiri, *Angew. Chem.* **1999**, 111, 1703; *Angew. Chem. Int. Ed.* **1999**, 38, 1598.
- [5] "Azobenzene-Containing Materials" (Ed.: A. Natansohn), *Macromol. Symp.* **1999**, 137, whole volume.
- [6] M. Matsumoto, S. Terretaz, H. Tachibana, *Adv. Colloid Interface Sci.* **2000**, 87, 147.
- [7] P. Cheben, F. del Monte, D. J. Worsfold, D. J. Carlsson, C. P. Grover, J. D. Mackenzie, *Nature* **2000**, 408, 64.
- [8] A. Altomare, F. Ciardelli, B. Gallot, M. Mader, R. Solaro, N. Tirelli, *J. Polym. Sci. Part A: Polym. Chem.* **2001**, 39, 2957.
- [9] R. Ballardini, V. Balzani, A. Credi, M. T. Gandolfi, M. Venturi, *Acc. Chem. Res.* **2001**, 34, 445.
- [10] V. Balzani, A. Credi, F. Marchioni, J. F. Stoddart, *Chem. Commun.* **2001**, 1860.
- [11] A. N. Shipway, I. Willner, *Acc. Chem. Res.* **2001**, 34, 421.
- [12] P. S. Ramanujam, N. C. R. Holme, M. Pedersen, S. Hvilsted, *J. Photochem. Photobiol. A* **2001**, 145, 49.
- [13] K. Weh, M. Noack, K. Hoffmann, K.-P. Schröder, J. Caro, *Microporous Mesoporous Mater.* **2002**, 54, 15.
- [14] N. Muranaka, T. Hoshaka, M. Sisido, *FEBS Lett.* **2002**, 510, 10.
- [15] A. S. Deonarine, S. M. Clark, L. Konermann, *Future Generation Computer Systems* **2003**, 19, 87.
- [16] G. Granucci, M. Persico, A. Toniolo, *J. Chem. Phys.* **2001**, 114, 10608.
- [17] M. Persico, G. Granucci, S. Inglese, T. Laino, A. Toniolo, *THEOCHEM* **2003**, 621, 119.
- [18] A. Toniolo, C. Ciminelli, G. Granucci, T. Laino, M. Persico, *Theoret. Chem. Acc.*, in press.
- [19] C. Ciminelli, G. Granucci, M. Persico, A. Toniolo, unpublished results.
- [20] J. Griffiths, *Chem. Soc. Rev.* **1972**, 1, 481.
- [21] H. Rau, in *P photochromism. Molecules and Systems*, (Eds.: H. Durr, H. Bouas-Laurent), Elsevier, Amsterdam, **1990**, Chapter 4, p. 165.
- [22] N. Tamai, H. Miyasaka, *Chem. Rev.* **2000**, 100, 1875.
- [23] W. Horspool, *The Chemistry of the Hydrazo, Azo and Azoxy Groups, Vol. 2* (Ed.: S. Patai), Wiley, **2000**.
- [24] S. Monti, G. Orlandi, P. Palmieri, *Chem. Phys.* **1982**, 71, 87.
- [25] H. Rau, E. Lüddecke, *J. Am. Chem. Soc.* **1982**, 104, 1616.
- [26] H. Rau, S. Yu-Quan, *J. Photochem. Photobiol. A* **1988**, 42, 321.
- [27] P. Cattaneo, M. Persico, *Phys. Chem. Chem. Phys.* **1999**, 1, 4739.
- [28] T. Ishikawa, T. Noro, T. Shoda, *J. Chem. Phys.* **2001**, 115, 7503.
- [29] E. W.-G. Diau, *J. Phys. Chem. A* **2004**, 108, 950.
- [30] L. Gagliardi, G. Orlandi, F. Bernardi, A. Cemran, M. Garavelli, *Theoret. Chem. Acc.*, in press.
- [31] G. Orlandi, private communication.
- [32] I. K. Lednev, T.-Q. Ye, R. E. Hester, J. N. Moore, *J. Phys. Chem.* **1996**, 100, 13338.
- [33] I. K. Lednev, T.-Q. Ye, P. Matousek, M. Towrie, P. Foggi, F. V. R. Neuwahl, S. Umapathy, R. E. Hester, J. N. Moore, *Chem. Phys. Lett.* **1998**, 290, 68.
- [34] T. Nägele, R. Hoche, W. Zinth, J. Wachtveitl, *Chem. Phys. Lett.* **1997**, 272, 489.
- [35] P. Hamm, S. M. Ohline, W. Zinth, *J. Chem. Phys.* **1997**, 106, 519.
- [36] T. Fujino, T. Tahara, *J. Phys. Chem. A* **2000**, 104, 4203.
- [37] T. Fujino, S. Yu. Arzhantsev, T. Tahara, *J. Phys. Chem. A* **2001**, 105, 8123.
- [38] T. Fujino, S. Yu. Arzhantsev, T. Tahara, *Bull. Chem. Soc. Jpn.* **2002**, 75, 1031.
- [39] Y.-C. Lu, C.-W. Chang, E. W.-G. Diau, *J. Chin. Chem. Soc.* **2002**, 49, 693.
- [40] H. Satzger, S. Spörlein, C. Root, J. Wachtveitl, W. Zinth, P. Gilch, *Chem. Phys. Lett.* **2003**, 372, 216.
- [41] T. Schultz, J. Quenneville, B. Levine, A. Toniolo, T. J. Martínez, S. Lochrunner, M. Schmitt, J. P. Schaffer, M. Z. Zgierski, A. Stolow, *J. Am. Chem. Soc.* **2003**, 125, 8098.
- [42] J. J. P. Stewart, MOPAC 2000, Fujitsu Limited, Tokio (Japan), **1999**.
- [43] J. C. Tully, *J. Chem. Phys.* **1990**, 93, 1061.
- [44] G. Granucci, A. Toniolo, *Chem. Phys. Lett.* **2000**, 325, 79.
- [45] P. Cattaneo, M. Persico, *J. Am. Chem. Soc.* **2001**, 123, 7638.
- [46] M. Terazima, M. Takezaki, S. Yamaguchi, N. Hirota, *J. Chem. Phys.* **1998**, 109, 603.
- [47] A. Toniolo, M. Persico, T. J. Martínez, unpublished results.
- [48] N. E. Petrachenko, V. I. Vovna, G. G. Furin, *J. Fluorine Chem.* **1993**, 63, 85.
- [49] M. J. S. Dewar, E. G. Zoebisch, E. F. Healy, J. J. P. Stewart, *J. Am. Chem. Soc.* **1985**, 107, 3902.
- [50] A. Toniolo, private communication.
- [51] A. Mostad, C. Romming, *Acta Chem. Scand.* **1971**, 25, 3561.
- [52] J. A. Bouwstra, A. Schouten, J. Kroon, *Acta Crystallogr. Sect. C* **1983**, 39, 1121.
- [53] M. Traettenberg, I. Hilmo, K. Hagen, *J. Mol. Struct.* **1977**, 39, 231.
- [54] T. Tsuji, H. Takashima, H. Takeuchi, T. Egawa, S. Konaka, *J. Phys. Chem. A* **2001**, 105, 9347.
- [55] N. Kurita, S. Tanaka, S. Itoh, *J. Phys. Chem. A* **2000**, 104, 8114.
- [56] P. C. Chen, Y. C. Chieh, *THEOCHEM* **2003**, 624, 191.
- [57] R. Cimraglia, H.-J. Hofmann, *Chem. Phys. Lett.* **1994**, 217, 430.
- [58] W. H. Press, S. A. Teukolsky, W. T. Vetterling, B. P. Flannery, *Numerical Recipes in Fortran 77*, Cambridge University Press, **1992**.
- [59] I. N. Ragazos, M. A. Robb, F. Bernardi, M. Olivucci, *Chem. Phys. Lett.* **1992**, 197, 217.
- [60] M. J. Bearpark, M. A. Robb, H. B. Schlegel, *Chem. Phys. Lett.* **1994**, 223, 269.
- [61] M. Riad Manaa, D. R. Yarkony, *J. Chem. Phys.* **1993**, 99, 5251.
- [62] D. R. Yarkony, *J. Chem. Phys.* **1996**, 104, 7866.
- [63] A. Toniolo, G. Granucci, T. J. Martínez, *J. Phys. Chem.* **2003**, 107, 3822.

Received: July 31, 2003 [F5415]